

## Article

# Monitoring the Spatio-Temporal Distribution of Soil Salinity Using Google Earth Engine for Detecting the Saline Areas Susceptible to Salt Storm Occurrence

Mohammad Kazemi Garajeh <sup>1,2</sup> 

<sup>1</sup> Department of Civil, Constructional and Environmental Engineering, Sapienza University of Rome, 00185 Rome, Italy; mohammad.kazemigarajeh@uniroma1.it

<sup>2</sup> School of Engineering, Università degli Studi della Basilicata, Via Nazario Sauro 85, 85100 Potenza, Italy

**Abstract:** Recent droughts worldwide have significantly affected ecosystems in various regions. Among these affected areas, the Lake Urmia Basin (LUB) has experienced substantial effects from both drought and human activity in recent years. Lake Urmia, known as one of the hypersaline lakes globally, has been particularly influenced by these activities. The extraction of water since 1995 has resulted in an increase in the extent of salty land, leading to the frequent occurrence of salt storms. To address this issue, the current study utilized various machine learning algorithms within the Google Earth Engine (GEE) platform to map the probability of saline storm occurrences. Landsat time-series images spanning from 2000 to 2022 were employed. Soil salinity indices, Ground Points (GPs), and Moderate Resolution Imaging Spectroradiometer (MODIS) aerosol products were utilized to prepare the training data, which served as input for constructing and running the models. The results demonstrated that the Support Vector Machine (SVM) performed effectively in identifying the probability of saline storm occurrence areas, achieving high  $R^2$  values of 91.12%, 90.45%, 91.78%, and 91.65% for the years 2000, 2010, 2015, and 2022, respectively. Additionally, the findings reveal an increase in areas exhibiting a very high probability of saline storm occurrences from 2000 to 2022. In summary, the results of this study indicate that the frequency of salt storms is expected to rise in the near future, owing to the increasing levels of soil salinity resources within the Lake Urmia Basin.

**Keywords:** soil salinity; salt storm; google earth engine; machine learning algorithms; Lake Urmia Basin



**Citation:** Kazemi Garajeh, M. Monitoring the Spatio-Temporal Distribution of Soil Salinity Using Google Earth Engine for Detecting the Saline Areas Susceptible to Salt Storm Occurrence. *Pollutants* **2024**, *4*, 1–15. <https://doi.org/10.3390/pollutants4010001>

Academic Editors: Mauro Marini and Raimundo Jimenez-Ballesta

Received: 27 July 2023

Revised: 26 November 2023

Accepted: 3 January 2024

Published: 8 January 2024



**Copyright:** © 2024 by the author. Licensee MDPI, Basel, Switzerland. This article is an open access article distributed under the terms and conditions of the Creative Commons Attribution (CC BY) license (<https://creativecommons.org/licenses/by/4.0/>).

## 1. Introduction

In recent years, humans have improperly exploited soil and water resources, leading to threatened ecosystems and sometimes unstable landforms and new-born ecosystems [1]. Wind-erodible sediment beds are one of the adverse consequences of the unprincipled exploitation of soil and water resources, leading to the disappearance of inland lakes and wetlands [2,3]. Soil salinity is a dynamic process with significant social and economic impacts, posing a threat to the communities exposed to it [4]. Soil salinity poses a significant environmental threat, particularly in arid and semiarid regions [5]. It is a detrimental consequence of irrigation and intensified agricultural practices, and represents a critical issue within the spectrum of soil degradation [6]. A high volume of soil salinity in an area easily allows saline storms to be created by unstable conditions [7,8].

Recent advancements in remote sensing have revolutionized the field of soil mapping, shifting from traditional methods to digital soil mapping. This transition has brought about more efficient and cost-effective tools for the widespread modeling and monitoring of soil salinity over large areas [9,10]. Moreover, the availability of remote sensing data with medium and high resolutions has further enhanced the capabilities of soil salinity detection [11]. Numerous studies have highlighted the considerable potential of Sentinel-2 and Landsat

images for modeling and mapping soil salinity [12–17]. These images have proven valuable in their contribution to understanding and monitoring soil salinity patterns.

Many indices have been developed for soil salinity detection using satellite-based datasets [18,19]. Spectral reflectance is a key factor in mapping soil salinity using soil salinity indices [20]. Nevertheless, it is important to consider various factors that can influence the spectral reflectance of satellite image bands when analyzing soil salinity. Physical features, chemical characteristics, soil color, moisture content, and surface roughness are among the factors that can impact spectral reflectance [21,22]. Additionally, saline soils with a dark, puffy surface crust tend to exhibit lower spectral reflectance [23]. These factors should be considered to ensure the accurate interpretation and assessment of soil salinity levels from satellite imagery.

Although spectral indices for mapping soil salinity using remote sensing have been employed in the domain of soil science, it is important to consider new platforms such as the Google Earth Engine (GEE) to update these approaches. The GEE offers enhanced capabilities for analyzing and mapping soil salinity distributions, providing opportunities to improve the accuracy and efficiency of inventory soil maps [24]. The GEE operates on cloud computing, utilizing Google's computational infrastructure and a vast collection of freely available remote sensing imagery with different resolutions. This powerful platform has found effective applications across various Earth science disciplines [25]. It has been utilized in deforestation analysis [26,27], land use mapping [28,29], monitoring the impacts of climate change [30], and air pollution monitoring [31,32]. One of the key features of the GEE is its ability to perform automated parallel processing, making use of Google's fast computing platform. This significantly reduces processing time and addresses the challenges associated with handling large volumes of data. The platform offers access to a wealth of free image information spanning 40 years, including imagery from the Sentinel series, Landsat, MODIS series, and more [33]. Given the widespread adoption of machine learning techniques in remote sensing, the GEE aims to facilitate the implementation of various machine learning algorithms. These algorithms can be broadly classified into four main groups [34]: (a) Statistical learning algorithms: This group includes methods such as Fast Naïve Bayes, which leverage statistical principles to make predictions. (b) Perceptron-based methods: This category encompasses algorithms like Winnow and Perceptron, which are based on the principles of neural networks and pattern recognition. (c) Logic-based algorithms: Algorithms like Random Forests, CART (Classification and Regression Trees), and Gmo Max Entropy fall under this group. They employ logical and decision tree-based approaches to analyze and classify remote sensing data. (d) Support Vector Machine (SVM) based algorithms: This group involves algorithms such as Margin SVM, Voting SVM, Pegasos, and IKPamir. SVM is a popular machine learning technique that utilizes geometric principles to separate and classify data [35–37]. Through the support of these machine learning algorithms, the GEE aims to enhance the capabilities of remote sensing data analysis and interpretation [28].

Machine learning algorithms and the GEE have gained significant popularity in geosciences due to their flexibility, performance, and high accuracy in modeling and predicting various phenomena [38]. The availability of large datasets has transformed the GEE into a powerful big data technology, further contributing to its growing prominence in the geoscience community. However, despite their widespread use, the comprehensive application and comparative analysis of machine learning techniques in the GEE have not been extensively addressed by previous researchers. As these innovative technologies are in a paradigm shift in the field of remote sensing, there is a need for more in-depth investigations into the efficiency and effectiveness of machine learning algorithms within the GEE framework. Specifically, there is a research gap in the detection of saline diffusion resources using the GEE and machine learning algorithms with spatial analysis. The absence of comprehensive studies in this area presents an opportunity for significant contributions to the field of remote sensing, representing a state-of-the-art research direction. Therefore, this study aims to identify and map the distribution of soil salinity in order

to detect the areas susceptible to salt storm in the LUB, Iran. To this end, Landsat series images as well as Moderate Resolution Imaging Spectroradiometer (MODIS) Aerosol Optical Depth (MCD19A2.061: Terra & Aqua MAIAC Land Aerosol Optical Depth Daily 1 km) were employed from 2000 to 2020.

## 2. Location of Study Area

The Lake Urmia Basin (LUB) is located in northwestern Iran (Figure 1). Lake Urmia is one of the largest hypersaline lakes in the world that covers a wide part of the LUB. In recent years, most of the lake has been become unusable land [39]. Drought and a rapid increase in agricultural activities are the most important reasons behind the shrinkage of the lake. These environmental changes may cause negative impacts such as the spread of diseases, destruction of agricultural lands, and massive damage to the local economy, resulting in the mass migration of local people, as has happened in the Aral Sea over the past decades [40].

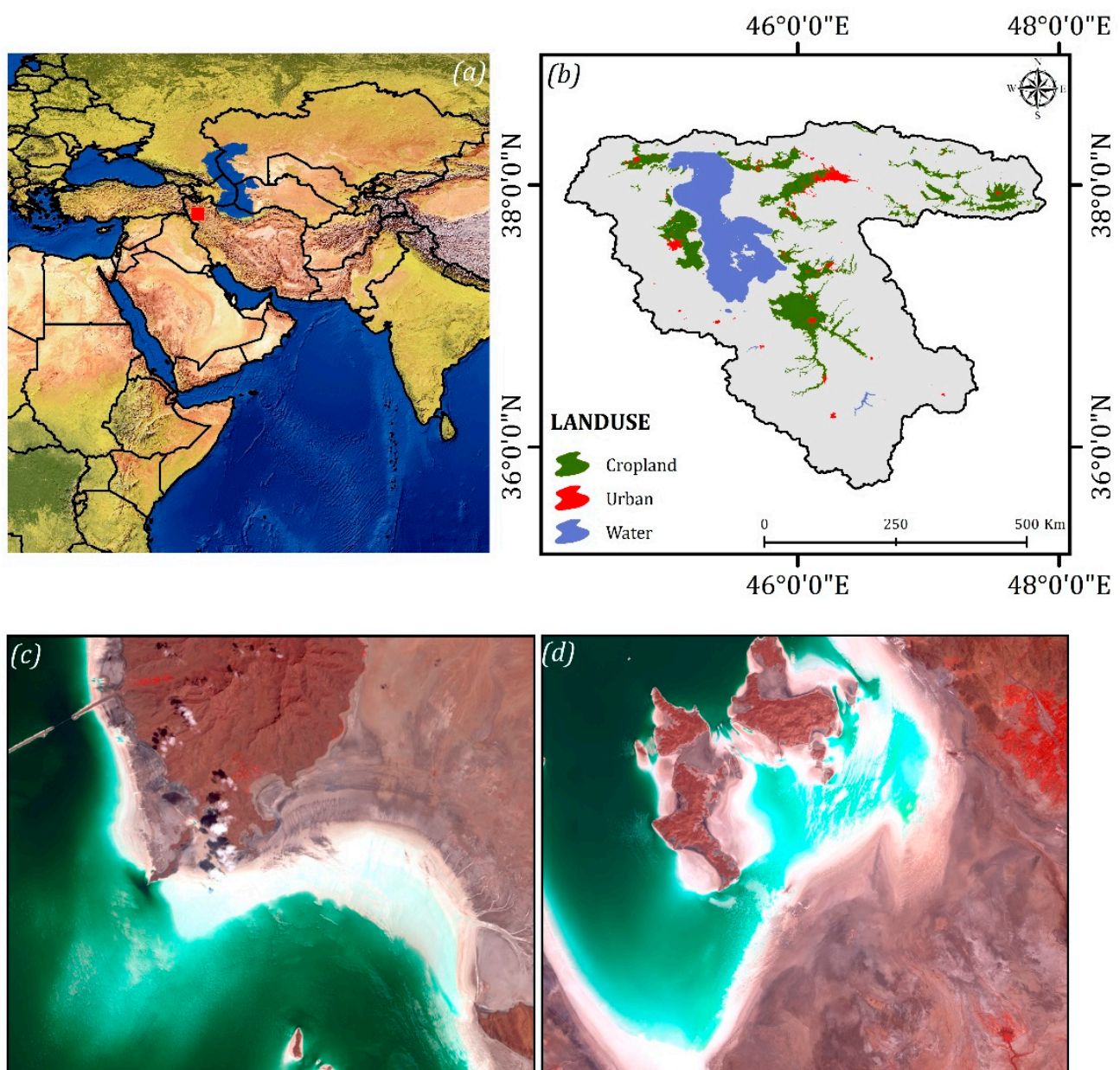


**Figure 1.** Location of study area in: (a) the world, (b) Iran. (c,d) are observed salt lands using Landsats 7 ETM+ and 8 OLI images for the years 2010 and 2013.

Over the past few decades, there has been a rapid decline in the volume of water in Lake Urmia. The lake's surface area has diminished significantly, reducing from 6100 square kilometers in 1995 to 953 square kilometers by August 2013 [41]. According to the Lake Urmia Restoration Program (LURP) announced in 2019, several factors have been identified as contributing to the drought of the lake. These include climate change, the increased discharge of groundwater for traditional irrigated agriculture, reduced precipitation, the construction of numerous dams, and the construction of a causeway across the lake. These factors have collectively played a role in the decline of water levels in the lake. Consequently, the shrinking of Lake Urmia since 1995 has resulted in noticeable and negative ecological changes in the surrounding areas. These changes include soil salinization, the salinization of groundwater, and an increase in the rate of saline dust [42].

### 3. Materials and Methodology

#### 3.1. Materials

In order to map and monitor the distribution of soil salinity and identify areas with a high potential for salt storms in the LUB, satellite images from Landsat 5 TM, 7 ETM+, and 8 OLI were utilized for the years 2000, 2010, 2015, and 2022. These images were specifically acquired for the month of August, which is known to be the driest month in the LUB [5]. Furthermore, all image processing was conducted in the GEE environment, which includes atmospheric correction for the images.

Ground Points (GPs) were collected at the end of the dry season from the study area where maximum salt accumulation exists in the topsoil. Based on real field observations, existing digital soil type, and land use/cover maps, a total of 1000 soil sampling points were selected for the years 2000, 2010, 2015, and 2022, respectively. A soil drill was used to collect and combine four topsoil samples (from 0 to 20 cm) at each sampling point. A portable global positioning system (GPS) device (UniStrong G120, with a positioning accuracy of  $\leq 5$  m) was also employed to record the geographic positions of the soil sampling points. All soil samples were appropriately sealed, labeled, and transported to the laboratory. The soil samples were completely air-dried. To eliminate non-soil materials, the soil samples passed through a 2 mm sieve. Finally, the soil electrical conductivity and soil-water ratio were determined at room temperature (25 °C) using a digital multi-parameter measuring instrument (Multi 3420 Set B, WTW GmbH, Munich, Germany) based on the prepared soil leachate at a 1:2.5 soil-to-water ratio. These GPs were divided into two groups, with 70% allocated for training the algorithms and 30% used for testing the accuracy of the machine learning results. Additionally, various soil salinity indexes (as shown in Table 1) were employed to create an inventory map for the training and validation process.

**Table 1.** Various soil salinity indexes used to generate an inventory map of soil salinity distribution.

Spectral Indexes	Acronym	Formula	References	R <sup>2</sup> (2000)	R <sup>2</sup> (2010)	R <sup>2</sup> (2015)	R <sup>2</sup> (2022)
Normalized difference salinity	NDSI	$(R - NIR)/(R + NIR)$	[18]	0.48	0.66	0.58	0.63
Salinity index 1	SI1	$(G \times R)^{0.5}$	[18]	0.63	0.79	0.56	0.48
Salinity index 2	SI2	$[(G)^2 + (R)^2 + (NIR)^2]^{0.5}$	[43]	0.66	0.68	0.85	0.88
Salinity index 3	SI3	$[(R)^2 + (G)^2]^{0.5}$	[19]	0.78	0.49	0.58	0.89
Salinity index I	S1	$B/R$	[18]	0.33	0.75	0.68	0.54
Salinity index II	S2	$(B - R)/(B + R)$	[19]	0.32	0.77	0.66	0.52
Salinity index III	S3	$(G \times R)/B$	[19]	0.55	0.75	0.73	0.69
Salinity index V	S5	$(B \times R)/G$	[18]	0.63	0.83	0.86	0.83
Salinity index VI	S6	$(R \times NIR)/G$	[18]	0.51	0.22	0.37	0.52

To enhance the accuracy of the results, data from the MODIS Aerosol Optical Depth (MCD19A2.061: Terra & Aqua MAIAC Land Aerosol Optical Depth Daily 1 km) were also incorporated in this study in the GEE environment. MCD19A2 is the shortname for the

Multi-Angle Implementation of Atmospheric Correction (MAIAC) algorithm-based Level-2 gridded (L2G) aerosol optical thickness over land surfaces product. Derived using both Terra and Aqua MODIS inputs, this L2 product is produced daily at a 1 km pixel resolution. This product helps generate a number of atmospheric and geometric properties/parameters that are used to produce another facet of the MAIAC algorithm: the land surface bidirectional reflectance factor (For more information, see the MAIAC user guide).

### 3.2. Methodology

This study utilized an integrated approach, combining remote sensing and GEE to monitor the probability of saline storm occurrence. The implementation of the entire study was conducted within the GEE environment. The first step involved the utilization of GPs and the generation of inventory maps using soil salinity indices and MODIS AOD products. These inventory maps were used to train and test the machine learning algorithms within the GEE platform. To validate the results obtained from the applied machine learning techniques, the k-fold cross-validation method was employed. This evaluation method helped assess the accuracy and effectiveness of the algorithms in predicting the soil salinity distribution and identifying areas prone to salt storm occurrences. An overview of the applied methodology to map soil salinity distribution and identify potential areas for salt storms is depicted in Figure 2.

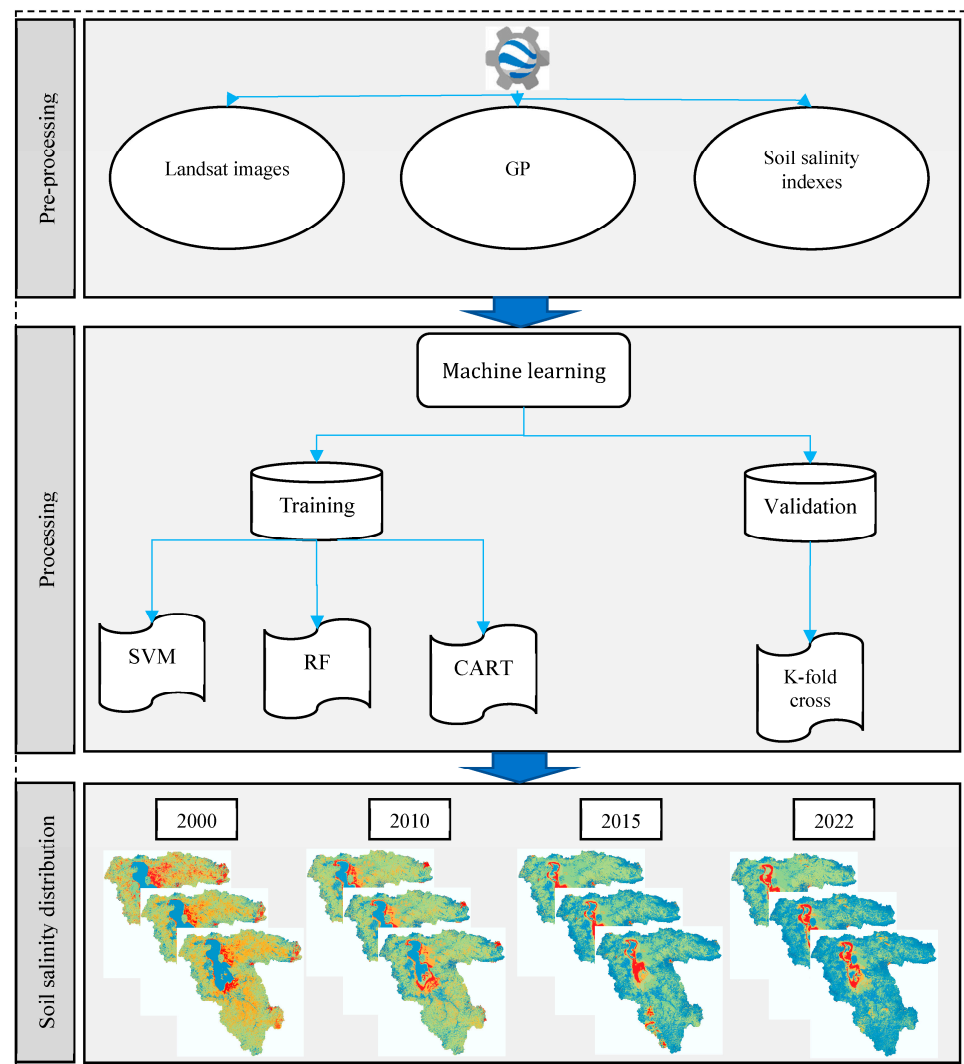


**Figure 2.** A summary of applied methodology for monitoring the distribution of soil salinity to detect the potential areas for salt storm occurrence.

### 3.2.1. Google Earth Engine

The data catalog of the GEE consists of numerous datasets commonly utilized by researchers, including the Landsat and Sentinel series images, and MODIS products (For more information, see <https://modis.gsfc.nasa.gov>, accessed on 1 August 2023). Additionally, there are lesser-known datasets such as hyperspectral data, night lights data, weather and climate data, and over 900 other datasets [44]. Users also have the option to upload their own data to the GEE server using the asset catalog. By collocating user data with the expanding GEE data catalog on the cloud, the integration and processing of data are expedited. The GEE's server-hosted data can be manipulated using a wide array of pre-loaded functions, algorithms, and tools, or by developing user-specific algorithms and functions tailored to their requirements [45]. The computational power of Google's servers and the active GEE developer community are leveraged to accomplish this. Notably, the high processing speeds offered by the platform enable the swift prototyping of new algorithms, allowing for efficient experimentation and the development of novel approaches [46]. Additionally, several machine learning algorithms are available in the GEE that are listed below:

### 3.2.2. Support Vector Machine (SVM)

Indeed, SVM is a supervised and non-parametric approach, and one of its significant strengths is its ability to produce good results even with a limited number of training samples. This attribute is particularly valuable in scenarios where obtaining a large, labeled dataset may be challenging or costly. SVM achieves this by effectively maximizing the margin, which is the distance between the decision boundary (hyperplane) and the support vectors [47]. By maximizing the margin, SVM aims to achieve better generalization and robustness to new, unseen data points. This property allows SVM to perform well in situations where the number of training samples is small compared to the complexity of the problem [48,49]. In essence, SVM's ability to handle limited training samples stems from its emphasis on finding the optimal separating hyperplane based on the support vectors. These support vectors capture the essential information required for classification, making SVM an effective approach even in cases where data availability is limited [50,51].

SVM employs various kernel functions, including linear, polynomial, radial basis function (RBF), and sigmoid. In this particular study, the RBF kernel was chosen due to its demonstrated superiority over other kernels and its widespread usage. The RBF kernel relies on two important parameters: 'cost' (C) and gamma [52,53]. The C parameter plays a crucial role in controlling the misclassification of training points. A higher value of C implies that fewer training points will be misclassified. On the other hand, the gamma parameter determines the 'spread' or reach of the kernel. A lower gamma value means that the influence of a single training sample extends farther, while a higher gamma value results in a more localized influence [54,55].

### 3.2.3. Random Forest (RF)

The RF classifier is a classification method based on ensemble learning, which aims to improve classification performance by constructing multiple classifiers instead of a single one [56]. The RF combines multiple decision trees that are independent of each other to create a robust model. Each decision tree undergoes its own evaluation process, and the results from these trees are averaged to produce the final output of the RF classifier. Decision trees, being weak learners, are combined to create a strong model [57]. RF can be used for predicting either class variables or regression variables [58,59]. In the GEE platform, there are six parameters related to RF that can be adjusted. These parameters included the number of trees, variables per split (with a default value of the square root of the number of variables), minimum leaf population (with a default value of 1), bag fraction (with a default value of 0.5), maximum nodes (with an unlimited default), and seed (with a default value of 0 for randomization). These parameter settings can be modified within the GEE platform to customize the RF classifier according to specific requirements [60,61].

### 3.2.4. Classification and Regression Trees (CART)

CART is a tree-based machine learning technique used for both regression and classification tasks [62]. It can handle numerical data for regression and categorical data for classification. The CART classifier constructs a decision tree by iteratively splitting the data at each node starting from the root. The training data are passed down the tree through these splits, and at each node, a decision is made to determine the next direction for the data. The decision is based on reducing the impurity at each node, which is determined by a splitting rule. For classification trees, common splitting rule metrics include the misclassification error, Gini index, entropy index, and twoing [63,64]. The splitting process continues until there is only one sample remaining, and a final decision is made at the terminal node, which represents the predicted class or regression value [65,66]. In the context of CART classifier implementation, the inputs typically consist of a feature collection representing the training data (70% of the data), a class property (e.g., 'Croplabel') that denotes the class labels, and input properties that encompass all the bands or features used for classification. In this regard, the GEE platform offers CART classification and regression algorithms. These algorithms require the definition of two parameters. The first parameter is 'maxNodes', which determines the maximum number of leaf nodes in the decision tree. By default, there is no limit on the maximum number of leaf nodes. The second parameter is 'minLeafPopulation', which specifies the minimum number of data points required to create new nodes during the construction of the decision tree. The default value for this parameter is one [67–69]. In the mentioned study, all the parameters for CART classification and regression were left as default values, meaning that the 'maxNodes' parameter had an unlimited value, and the 'minLeafPopulation' parameter was set to one.

### 3.3. Accuracy Assessment

In this study, a k-fold cross-validation method was employed. This method involves dividing the samples into k evenly sized folds. During each iteration, k – 1 folds were utilized for training the model, while the remaining fold was used for validation. This process was repeated k times, ensuring that each fold served as both a validation set and a training set. Following k iterations, the regression results were averaged to obtain the final outcome [32]. To evaluate the performance of the model, two metrics were utilized: the root mean square error (RMSE) and R-squared ( $R^2$ ). These metrics were calculated at every iteration, and the average of all the iteration results was used to determine the accuracy of the model [70]. The equations below illustrate the calculation of RMSE and  $R^2$ , respectively:

$$RMSE = \sqrt{\frac{1}{n} \sum_{i=1}^n (X_i - Y_i)^2} \quad (1)$$

$$R^2 = 1 - \frac{\sum_{i=1}^n (X_i - Y_i)^2}{\sum_{i=1}^n (X_i - \bar{X}_i)^2} \quad (2)$$

where  $n$  is sample size,  $X_i$  is measured soil salinity value,  $Y_i$  is the predicted soil salinity value, and  $\bar{X}_i$  is the average of the measured soil salinity values.

Table 2 shows the results of the k-fold cross validation method for monitoring the distribution of soil salinity to identify the potential areas for salt storm occurrence. According to Table 2, the SVM machine performed well with an  $R^2$  of 91.12%, 90.45%, 91.78%, and 91.65% for the years 2000, 2010, 2015, and 2022, respectively, compared to RF and CART.

**Table 2.** Results of the k-fold cross validation method.

Year	SVM		RF		CART	
	R <sup>2</sup>	RMSE	R <sup>2</sup>	RMSE	R <sup>2</sup>	RMSE
2000	91.12	4.21	87.36	5.89	85.65	6.65
2010	90.45	4.89	86.78	6.42	85.11	6.87
2015	91.78	3.99	87.12	6.24	84.99	7.12
2022	91.65	4.09	87.01	6.13	85.21	6.94

#### 4. Results

This study aimed to monitor the distribution of soil salinity and identify potential areas for salt storm occurrences using machine learning algorithms in the GEE environment. Three machine learning algorithms, namely SVM, RF, and CART, were utilized in the GEE for this purpose. Figure 3 depicts the distribution of soil salinity in the LUB from 2000 to 2022.

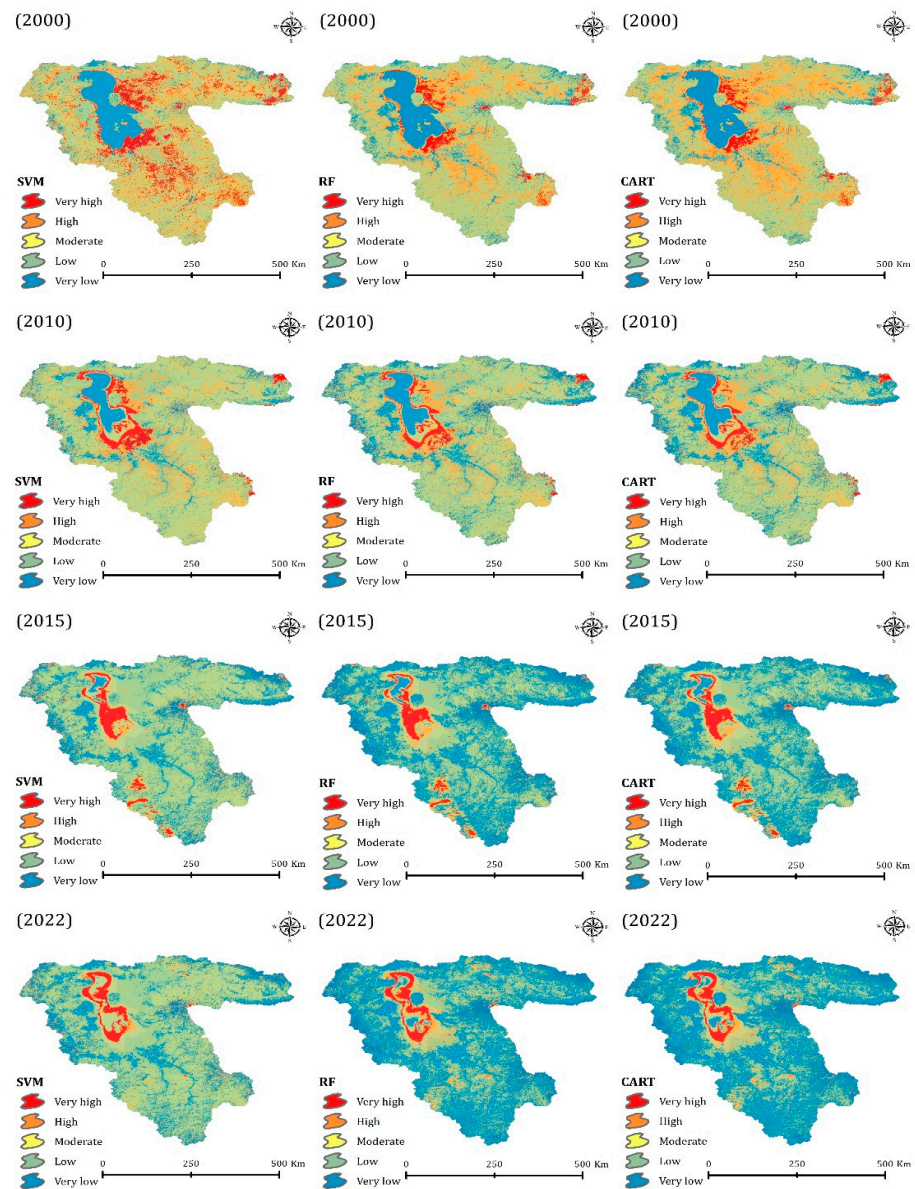


**Figure 3.** Spatio-temporal probability of saline storm occurrences, generated using machine learning algorithms in the GEE for the years 2000, 2010, 2015, and 2022.

This study found that SVM performed well in monitoring the probability of saline storm occurrences compared to RF and CART, as indicated in Table 2. The results revealed an increasing trend in the probability of saline storm occurrences in the LUB from 2000 to 2022. The maps generated using machine learning algorithms consistently showed an increase in areas with very high concentrations of soil salinity throughout this period (Table 3). Notably, the highest increase in soil salinity concentration occurred in 2015 when the lake experienced significant drying.

**Table 3.** Spatio-temporal probability of saline storm occurrences in %, generated using machine learning algorithms in the GEE for the years 2000, 2010, 2015, and 2022.

		2000			2010		
Class	SVM	RF	CART	Class	SVM	RF	CART
Very low	12.00	16.20	16.22	Very low	12.93	21.42	23.79
Low	47.47	56.88	47.20	Low	66.10	60.92	58.55
Moderate	29.93	23.88	33.54	Moderate	16.17	14.50	14.65
High	9.54	2.12	2.12	High	3.71	2.00	1.76
Very high	1.07	0.92	0.92	Very high	1.09	1.17	1.26
		2015			2022		
Class	SVM	RF	CART	Class	SVM	RF	CART
Very low	26.64	50.38	49.07	Very low	28.53	62.21	65.96
Low	67.08	43.02	44.33	Low	66.35	30.60	26.85
Moderate	2.51	3.29	3.30	Moderate	1.97	4.30	4.30
High	2.44	1.60	1.59	High	1.86	1.58	1.58
Very high	1.33	1.70	1.70	Very high	1.29	1.32	1.32

However, it is mentioned that the areas with a high distribution of soil salinity decreased, which contributed to the overall increase in very high distribution of soil salinization in the LUB from 2000 to 2022. In summary, this study's findings indicate that the areas with the highest soil salinity levels increased during the period from 2000 to 2022, consequently increasing the potential for salt storms in those areas.

In addition to monitoring the probability of saline storm occurrences, this study also utilized the MODIS AOD product to track the time series of dust storms over the study area from 2000 to 2022. Table 4 provides insights into the changes observed in the thickness of dust over the LUB during this period. According to the data presented in Table 4, the thickness of dust over the LUB in August 2000 was recorded as 0.285. Over the years, there was an increase in the thickness of dust, with the value reaching 0.416 in August 2010. Subsequently, in August 2015, the AOD thickness further increased to 0.423. By August 2022, the MODIS AOD product indicated a recorded value of approximately 0.459 for the AOD thickness.

**Table 4.** The thickness of AOD over study area from 2000 to 2022 in August.

Product Name	2000	2010	2015	2022
AOD thickness	0.285	0.416	0.423	0.459

These results suggest that there has been a general increasing trend in the thickness of dust storms over the study area from 2000 to 2022. The data show a gradual rise in AOD thickness, indicating an escalation in the intensity or frequency of dust storms in the LUB region over time. Table 5 also shows an  $R^2$  of 0.69, 0.69, and 0.73 between the very high class for the concentration of soil salinity and aerosol thickness from 2000 to 2022. The results of the

correlation coefficient show that an increase in the distribution of soil salinity would increase the thickness of aerosol, which accordingly increases the frequency of salt storms.

**Table 5.** Correlation coefficient between the distribution of soil salinity and aerosol thickness from 2000 to 2022.

Methods	SVM	RF	CART
R <sup>2</sup>	0.69	0.69	0.73

## 5. Discussion

### 5.1. General Discussion

In recent years, salt storms have become an unexpected natural disaster that occurs within the territory of the LUB due to the significant drying of Lake Urmia. To address this issue, this study employed three machine learning algorithms: SVM, RF, and CART, in conjunction with the MODIS AOD product. The goal was to analyze the probability of saline storm occurrences in the LUB. This study's results indicate that the potential for salt storms in the LUB has increased due to the rising distribution of soil salinity from 2000 to 2022. Furthermore, the findings highlight machine learning algorithms as promising techniques for detecting the probability of saline storm occurrences on a large scale.

### 5.2. Probability of Saline Storm Occurrences from 2000 to 2022

As mentioned, the probability of saline storm occurrences increased from 2000 to 2022 in the LUB, as shown in Table 3. This increase is consistent with the values derived from the MODIS AOD product, as presented in Table 4. According to Table 3, the very high probability of saline storm occurrence was 1.07%, 1.09%, 1.33%, and 1.29% for the years 2000, 2010, 2015, and 2022, respectively. This probability class increased by approximately 0.22% from 2000 to 2022. We considered the SVM results because it demonstrated the highest performance in mapping the probability of saline storm occurrence compared to other techniques. The high probability of saline storm occurrence was estimated to be 9.54%, 3.71%, 2.44%, and 1.86% for the years 2000, 2010, 2015, and 2022, respectively, as shown in Table 3. According to these results, there is a reduction in the class with a high probability of saline storm occurrences from 2000 to 2022, which aligns with the increase in the class with very high probability of saline storm occurrences. The results of this research reveal that 1.07%, 1.09%, 1.33%, and 1.29% of the LUB area faced a very high probability of saline storm occurrences for the years 2000, 2010, 2015, and 2022, respectively. This could be a direct result of the recent dryness in Lake Urmia. The period from 2005 to 2015 was the driest on record and led to a sharp drop in the water level, decreasing it by more than seven meters [71]. According to the Department of Environment (DOE) in 2010, a water level of 1274.1 m above sea level would be necessary for the lake to maintain its normal ecological function and preserve its environmental diversity. However, based on the West Azerbaijan Regional Water Organization's report, the water level of Urmia Lake decreased from 1275.74 m in 1978 to 1270.91 m in 2012. Figure 3 illustrates that areas with a high probability of saline storm occurrence are located on the eastern and southern shores of Urmia Lake. This distribution is attributed to the lower slope angles of these shores in comparison to other regions [17]. Table 3 reveals that 29.93%, 16.17%, 2.51%, and 1.97% of the study area face a moderate probability of saline storm occurrences for the years 2000, 2010, 2015, and 2022, respectively. These areas are predominantly found in the eastern and southern parts of the Urmia Lake area, primarily due to the prevalence of barren land and abandoned agricultural areas affected by soil salinity. Additionally, 47.47%, 66.10%, 67.08%, and 66.35% of the LUB exhibit a low probability of saline storm occurrences for the years 2000, 2010, 2015, and 2022, respectively, while 12.00%, 12.93%, 26.64%, and 28.53% have a very low probability of saline storm occurrence for the years 2000, 2010, 2015, and 2022 (Table 3). The analysis of electrical conductivity (EC) also indicates that the average EC for 218 GCPs was 3.68 in the year 2000. This value rises to 5.09 in 2010 for 217 GCPs.

Furthermore, the electrical analysis uncovers an EC mean value of 6.98 in 2015 for 278 GCPs. The EC mean value for GCPs in 2022, numbering 287, is 6.65. This illustrates a notable increase of 2.97 in EC from the year 2000 to 2022.

### *5.3. Efficiency of Remote Sensing and GEE for Modeling the Probability of Saline Storm Occurrence*

Traditional satellite-based approaches for soil salinity distribution rely on spectral indexes, as outlined in Table 1. According to [72], soil salinity information obtained from satellite images can be influenced by terrestrial and atmospheric factors. Consequently, it is imperative to employ advanced methods to mitigate the impact of these factors. GEE, an online platform that provides access to a diverse array of global satellite images and offers image-processing and -classification capabilities, leverages contemporary methods like machine learning and deep learning techniques. The results of this study affirm that GEE is well suited for harnessing vast amounts of data and can serve as a testbed for various machine learning algorithms. Monitoring the soil salinity distribution from remote sensing images poses a challenge due to the diverse elements involved and their complex spatial and spectral characteristics. However, this study successfully addresses these complexities through the application of automated data-driven approaches. By demonstrating the applicability of different machine learning algorithms within the GEE platform, this study provides a comprehensive framework for monitoring various earth features, including soil salinity distribution, at different scales and levels.

### *5.4. The Effects of Saline Storms on the Local Environment and Inhabitation*

Soil salinity can have various impacts on different aspects of the environment and human activities. The following are some of the key impacts of soil salinity: The expansion of salt-affected areas: High soil salinity can contribute to the expansion of salt-affected areas, which can lead to the formation of salt storms. When the soil becomes saline, the salts can be carried by wind and deposited on nearby areas, causing damage to vegetation, infrastructure, and affecting the overall ecosystem. Agricultural productivity loss: Soil salinity poses a significant threat to agriculture. High salt levels in the soil can hinder the germination, growth, and development of plants, leading to reduced crop yields and economic losses for farmers. Salinity also affects the availability of water to plants, as excessive salt levels can disrupt the water balance in plant cells. Soil degradation and desertification: Persistent soil salinity can contribute to soil degradation and desertification. Excessive salt accumulation can degrade soil structure, reduce its fertility, and make it less suitable for plant growth. Over time, this can lead to the loss of topsoil, erosion, and the conversion of productive land into barren, salt-affected areas. Impact on ecosystems: Soil salinity can have negative effects on natural ecosystems. It can disrupt the balance of plant and animal species adapted to specific soil conditions, leading to changes in biodiversity and potentially causing a decline in or loss of certain species. Salinity can also impact water bodies, as a high salt content in the soil can leach into groundwater or runoff into rivers, affecting aquatic ecosystems. Health concerns: In areas affected by soil salinity, the salts can contaminate water sources, making them unsuitable for human consumption. Additionally, the inhalation of salt particles carried by wind during salt storms can have adverse effects on respiratory health. Moreover, the lack of suitable agricultural areas due to soil salinity can contribute to food insecurity and malnutrition in affected regions. To mitigate these impacts, it is crucial to monitor and map soil salinity distribution, as mentioned earlier. This information can help in developing strategies for soil management, irrigation techniques, crop selection, and land use planning to minimize the negative effects of soil salinity and promote sustainable land and water management practices.

### *5.5. Limitation of the Present Research*

The potential applications of learning-based approaches are nearly limitless. In the context of mapping the probability of saline storm occurrences, further research is essential

to gain a better understanding of the dynamic nature of saline storms, allowing for the simulation of their variations and effects in semi-arid and arid regions.

## 6. Conclusions

In this study, we employed machine learning algorithms such as SVM, RF, and CART to effectively monitor the distribution of soil salinity and identify potential areas for salt storm occurrences in the LUB region. The findings indicate that SVM performed well with an  $R^2$  of 91.12%, 90.45%, 91.78%, and 91.65% for the years 2000, 2010, 2015, and 2022, respectively, compared to RF and CART in monitoring soil salinity distribution in the area of interest. Furthermore, the results reveal an increasing trend in the potential areas for salt storm occurrence from 2000 to 2022 in the LUB. This is especially evident in the class with a very high probability of salt storm occurrences, showing an increase of 0.22% for SVM, 0.4% for RF, and 0.4% the CART from 2000 to 2022. This highlights the importance of continuous monitoring and the assessment of soil salinity to better understand and predict the occurrence of salt storms. The results also show a gradual rise in AOD thickness of 0.174 from 2000 to 2022, indicating an escalation in the intensity or frequency of dust storms in the LUB region over time. This study found that the use of cloud-free platforms like the GEE provides easy access to a wide range of datasets, eliminating the need for extensive pre-processing stages. This integration of remote sensing datasets with the GEE platform proved highly effective in monitoring and mapping the dynamic nature of soil salinization over large areas. Overall, the results of this study offer insights and practical applications for researchers, planners, and administrators, enabling them to identify areas most affected by salinity and predict potential areas at risk of salt storms.

**Funding:** This research received no external funding.

**Institutional Review Board Statement:** Not applicable.

**Informed Consent Statement:** Not applicable.

**Data Availability Statement:** The data presented in this study are available upon request from the corresponding author.

**Conflicts of Interest:** The author declares no conflict of interest.

## References

1. Bannari, A.; Guedon, A.M.; El-Harti, A.; Cherkaoui, F.Z.; El-Ghmari, A. Characterization of slightly and moderately saline and sodic soils in irrigated agricultural land using simulated data of advanced land imaging (EO-1) sensor. *Commun. Soil Sci. Plant Anal.* **2008**, *39*, 2795–2811. [\[CrossRef\]](#)
2. Asfaw, E.; Suryabhagavan, K.V.; Argaw, M. Soil salinity modeling and mapping using remote sensing and GIS: The case of Wonji sugar cane irrigation farm, Ethiopia. *J. Saudi Soc. Agric. Sci.* **2018**, *17*, 250–258. [\[CrossRef\]](#)
3. Gorji, T.; Sertel, E.; Tanik, A. Monitoring soil salinity via remote sensing technology under data scarce conditions: A case study from Turkey. *Ecol. Indic.* **2017**, *74*, 384–391. [\[CrossRef\]](#)
4. El Hafyani, M.; Essahlaoui, A.; El Baghdadi, M.; Teodoro, A.C.; Mohajane, M.; El Hmairi, A.; El Ouali, A. Modeling and mapping of soil salinity in Tafilalet plain (Morocco). *Arab. J. Geosci.* **2019**, *12*, 35. [\[CrossRef\]](#)
5. Kazemi Garajeh, M.; Malakyar, F.; Weng, Q.; Feizizadeh, B.; Blaschke, T.; Lakes, T. An automated deep learning convolutional neural network algorithm applied for soil salinity distribution mapping in Lake Urmia, Iran. *Sci. Total Environ.* **2021**, *778*, 146253. [\[CrossRef\]](#)
6. Moreira, L.C.J.; Teixeira, A.D.S.; Galvão, L.S. Potential of multispectral and hyperspectral data to detect saline-exposed soils in Brazil. *GIScience Remote Sens.* **2015**, *52*, 416–436. [\[CrossRef\]](#)
7. Ivits, E.; Cherlet, M.; Tóth, T.; Lewińska, K.E.; Tóth, G. Characterisation of productivity limitation of salt-affected lands in different climatic regions of Europe using remote sensing derived productivity indicators. *Land Degrad. Dev.* **2013**, *24*, 438–452. [\[CrossRef\]](#)
8. Elhag, M. Evaluation of different soil salinity mapping using remote sensing techniques in arid ecosystems, Saudi Arabia. *J. Sens.* **2016**, *2016*, 7596175. [\[CrossRef\]](#)
9. Metternicht, G.I.; Zinck, J.A. Remote sensing of soil salinity: Potentials and constraints. *Remote Sens. Environ.* **2003**, *85*, 1–20. [\[CrossRef\]](#)
10. Taghadosi, M.M.; Hasanlou, M.; Eftekhari, K. Soil salinity mapping using dual-polarized SAR Sentinel-1 imagery. *Int. J. Remote Sens.* **2019**, *40*, 237–252. [\[CrossRef\]](#)

11. Omrani, M.; Shahbazi, F.; Feizizadeh, B.; Oustan, S.; Najafi, N. Application of remote sensing indices to digital soil salt composition and ionic strength mapping in the east shore of Urmia Lake, Iran. *Remote Sens. Appl. Soc. Environ.* **2021**, *22*, 100498. [[CrossRef](#)]
12. Yu, H.; Liu, M.; Du, B.; Wang, Z.; Hu, L.; Zhang, B. Mapping soil salinity/sodicity by using Landsat OLI imagery and PLSR algorithm over semiarid West Jilin Province, China. *Sensors* **2018**, *18*, 1048. [[CrossRef](#)] [[PubMed](#)]
13. Wang, J.; Ding, J.; Yu, D.; Ma, X.; Zhang, Z.; Ge, X.; Teng, D.; Li, X.; Liang, J.; Lizaga, I.; et al. Capability of Sentinel-2 MSI data for monitoring and mapping of soil salinity in dry and wet seasons in the Ebinur Lake region, Xinjiang, China. *Geoderma* **2019**, *353*, 172–187. [[CrossRef](#)]
14. Davis, E.; Wang, C.; Dow, K. Comparing Sentinel-2 MSI and Landsat 8 OLI in soil salinity detection: A case study of agricultural lands in coastal North Carolina. *Int. J. Remote Sens.* **2019**, *40*, 6134–6153. [[CrossRef](#)]
15. Taghadosi, M.M.; Hasanlou, M.; Eftekhari, K. Retrieval of soil salinity from Sentinel-2 multispectral imagery. *Eur. J. Remote Sens.* **2019**, *52*, 138–154. [[CrossRef](#)]
16. Nguyen, K.A.; Liou, Y.A.; Tran, H.P.; Hoang, P.P.; Nguyen, T.H. Soil salinity assessment by using near-infrared channel and Vegetation Soil Salinity Index derived from Landsat 8 OLI data: A case study in the Tra Vinh Province, Mekong Delta, Vietnam. *Prog. Earth Planet. Sci.* **2020**, *7*, 126489. [[CrossRef](#)]
17. Gorji, T.; Yildirim, A.; Hamzehpour, N.; Tanik, A.; Sertel, E. Soil salinity analysis of Urmia Lake Basin using Landsat-8 OLI and Sentinel-2A based spectral indices and electrical conductivity measurements. *Ecol. Indic.* **2020**, *112*, 106173. [[CrossRef](#)]
18. Khan, N.M.; Rastoskuev, V.V.; Sato, Y.; Shiozawa, S. Assessment of hydrosaline land degradation by using a simple approach of remote sensing indicators. *Agric. Water Manag.* **2005**, *77*, 96–109. [[CrossRef](#)]
19. Douaoui, A.; Nicolas, H.; Walter, C. Detecting salinity hazards within a semiarid context by means of combining soil and remote-sensing data. *Geoderma* **2006**, *134*, 217–230. [[CrossRef](#)]
20. Yahiaoui, I.; Douaoui, A.; Zhang, Q.; Ziane, A. Soil salinity prediction in the Lower Cheliff plain (Algeria) based on remote sensing and topographic feature analysis. *J. Arid Land* **2015**, *7*, 794–805. [[CrossRef](#)]
21. Jafari, A.; Khademi, H.; Finke, P.A.; Van de Wauw, J.; Ayoubi, S. Spatial prediction of soil great groups by boosted regression trees using a limited point dataset in an arid region, southeastern Iran. *Geoderma* **2014**, *232*, 148–163. [[CrossRef](#)]
22. Meier, M.; Souza, E.D.; Francelino, M.R.; Fernandes Filho, E.I.; Schaefer, C.E.G.R. Digital soil mapping using machine learning algorithms in a tropical mountainous area. *Rev. Bras. Ciência Solo* **2018**, *42*, e0170421. [[CrossRef](#)]
23. Shahabi, M.; Jafarzadeh, A.A.; Neyshabouri, M.R.; Ghorbani, M.A.; Valizadeh Kamran, K. Spatial modeling of soil salinity using multiple linear regression, ordinary kriging and artificial neural network methods. *Arch. Agron. Soil Sci.* **2017**, *63*, 151–160. [[CrossRef](#)]
24. Ma, S.; He, B.; Ge, X.; Luo, X. Spatial prediction of soil salinity based on the Google Earth Engine platform with multitemporal synthetic remote sensing images. *Ecol. Inform.* **2023**, *75*, 102111. [[CrossRef](#)]
25. Kazemi Garajeh, M.; Laneve, G.; Rezaei, H.; Sadeghnejad, M.; Mohamadzadeh, N.; Salmani, B. Monitoring Trends of CO<sub>2</sub>, NO<sub>2</sub>, SO<sub>2</sub>, and O<sub>3</sub> Pollutants Using Time-Series Sentinel-5 Images Based on Google Earth Engine. *Pollutants* **2023**, *3*, 255–279. [[CrossRef](#)]
26. Chen, S.; Woodcock, C.E.; Bullock, E.L.; Arévalo, P.; Torchinava, P.; Peng, S.; Olofsson, P. Monitoring temperate forest degradation on Google Earth Engine using Landsat time series analysis. *Remote Sens. Environ.* **2021**, *265*, 112648. [[CrossRef](#)]
27. da Silva, M.V.; Pandorfi, H.; de Oliveira-Júnior, J.F.; da Silva, J.L.B.; de Almeida, G.L.P.; de Assunção Montenegro, A.A.; Mesquita, M.; Ferreira, M.B.; Santana, T.C.; Marinho, G.T.B.; et al. Remote sensing techniques via Google Earth Engine for land degradation assessment in the Brazilian semiarid region, Brazil. *J. South Am. Earth Sci.* **2022**, *120*, 104061. [[CrossRef](#)]
28. Zurqani, H.A.; Post, C.J.; Mikhailova, E.A.; Schlautman, M.A.; Sharp, J.L. Geospatial analysis of land use change in the Savannah River Basin using Google Earth Engine. *Int. J. Appl. Earth Obs. Geoinf.* **2018**, *69*, 175–185. [[CrossRef](#)]
29. Liang, J.; Chen, C.; Song, Y.; Sun, W.; Yang, G. Long-term mapping of land use and cover changes using Landsat images on the Google Earth Engine Cloud Platform in bay area-A case study of Hangzhou Bay, China. *Sustain. Horiz.* **2023**, *7*, 100061. [[CrossRef](#)]
30. Kazemi Garajeh, M.; Salmani, B.; Zare Naghadehi, S.; Valipoori Goodarzi, H.; Khasraei, A. An integrated approach of remote sensing and geospatial analysis for modeling and predicting the impacts of climate change on food security. *Sci. Rep.* **2023**, *13*, 1057. [[CrossRef](#)]
31. Aghazadeh, F.; Ghasemi, M.; Garajeh, M.K.; Feizizadeh, B.; Karimzadeh, S.; Morsali, R. An integrated approach of deep learning convolutional neural network and google earth engine for salt storm monitoring and mapping. *Atmos. Pollut. Res.* **2023**, *14*, 101689. [[CrossRef](#)]
32. Kazemi Garajeh, M.; Li, Z.; Hasanlu, S.; Zare Naghadehi, S.; Hossein Haghi, V. Developing an integrated approach based on geographic object-based image analysis and convolutional neural network for volcanic and glacial landforms mapping. *Sci. Rep.* **2022**, *12*, 21396. [[CrossRef](#)]
33. Feizizadeh, B.; Garajeh, M.K.; Lakes, T.; Blaschke, T. A deep learning convolutional neural network algorithm for detecting saline flow sources and mapping the environmental impacts of the Urmia Lake drought in Iran. *Catena* **2021**, *207*, 105585. [[CrossRef](#)]
34. Mahdianpari, M.; Brisco, B.; Salehi, B.; Granger, J.; Mohammadimanesh, F.; Lang, M.; Toure, S. Toward a North American continental wetland map from space: Wetland classification using satellite imagery and machine learning algorithms on Google Earth Engine. In *Radar Remote Sensing*; Elsevier: Amsterdam, The Netherlands, 2022; pp. 357–373.
35. Chen, H.; Yunus, A.P.; Nukapothula, S.; Avtar, R. Modelling Arctic coastal plain lake depths using machine learning and Google Earth Engine. *Phys. Chem. Earth Parts A/B/C* **2022**, *126*, 103138. [[CrossRef](#)]

36. Waleed, M.; Sajjad, M.; Shazil, M.S.; Tariq, M.; Alam, M.T. Machine learning-based spatial-temporal assessment and change transition analysis of wetlands: An application of Google Earth Engine in Sylhet, Bangladesh (1985–2022). *Ecol. Inform.* **2023**, *75*, 102075. [[CrossRef](#)]
37. Imanni, H.S.; El Harti, A.; Bachaoui, E.M.; Mouncif, H.; Eddassouqui, F.; Hasnai, M.A.; Zinelabidine, M.I. Multispectral UAV data for detection of weeds in a citrus farm using machine learning and Google Earth Engine: Case study of Morocco. *Remote Sens. Appl. Soc. Environ.* **2023**, *30*, 100941.
38. Feizizadeh, B.; Omarzadeh, D.; Kazemi Garajeh, M.; Lakes, T.; Blaschke, T. Machine learning data-driven approaches for land use/cover mapping and trend analysis using Google Earth Engine. *J. Environ. Plan. Manag.* **2023**, *66*, 665–697. [[CrossRef](#)]
39. Ahmadi, H.; Argany, M.; Ghanbari, A.; Ahmadi, M. Visualized spatiotemporal data mining in investigation of Urmia Lake drought effects on increasing of PM10 in Tabriz using Space-Time Cube (2004–2019). *Sustain. Cities Soc.* **2022**, *76*, 103399. [[CrossRef](#)]
40. Abbasian, M.S.; Najafi, M.R.; Abrishamchi, A. Increasing risk of meteorological drought in the Lake Urmia basin under climate change: Introducing the precipitation–temperature deciles index. *J. Hydrol.* **2021**, *592*, 125586. [[CrossRef](#)]
41. Amirataee, B.; Montaseri, M.; Rezaie, H. Regional analysis and derivation of copula-based drought Severity–Area–Frequency curve in Lake Urmia basin, Iran. *J. Environ. Manag.* **2018**, *206*, 134–144. [[CrossRef](#)]
42. Pouladi, P.; Badiadzadeh, S.; Pouladi, M.; Yousefi, P.; Farahmand, H.; Kalantari, Z.; Yu, D.J.; Sivapalan, M. Interconnected governance and social barriers impeding the restoration process of Lake Urmia. *J. Hydrol.* **2021**, *598*, 126489. [[CrossRef](#)]
43. Abbas, A.; Khan, S. Using remote sensing techniques for appraisal of irrigated soil salinity. In *International Congress on Modelling and Simulation (MODSIM)*; Modelling and Simulation Society of Australia and New Zealand: Christchurch, New Zealand, 2007; pp. 2632–2638.
44. You, N.; Dong, J. Examining earliest identifiable timing of crops using all available Sentinel 1/2 imagery and Google Earth Engine. *ISPRS J. Photogramm. Remote Sens.* **2020**, *161*, 109–123. [[CrossRef](#)]
45. Thieme, A.; Yadav, S.; Oddo, P.C.; Fitz, J.M.; McCartney, S.; King, L.; Keppler, J.; McCarty, G.W.; Hively, W.D. Using NASA Earth observations and Google Earth Engine to map winter cover crop conservation performance in the Chesapeake Bay watershed. *Remote Sens. Environ.* **2020**, *248*, 111943. [[CrossRef](#)]
46. Sulova, A.; Jokar Arsanjani, J. Exploratory analysis of driving force of wildfires in Australia: An application of machine learning within Google Earth engine. *Remote Sens.* **2020**, *13*, 10. [[CrossRef](#)]
47. Vapnik, V. *The Nature of Statistical Learning Theory*; Springer: New York, NY, USA, 1995.
48. Chung, L.C.H.; Xie, J.; Ren, C. Improved machine-learning mapping of local climate zones in metropolitan areas using composite Earth observation data in Google Earth Engine. *Build. Environ.* **2021**, *199*, 107879. [[CrossRef](#)]
49. Zhang, Q.; Xiao, J.; Tian, C.; Chun-Wei Lin, J.; Zhang, S. A robust deformed convolutional neural network (CNN) for image denoising. *CAAI Trans. Intell. Technol.* **2023**, *8*, 331–342. [[CrossRef](#)]
50. Cao, J.; Zhang, Z.; Luo, Y.; Zhang, L.; Zhang, J.; Li, Z.; Tao, F. Wheat yield predictions at a county and field scale with deep learning, machine learning, and google earth engine. *Eur. J. Agron.* **2021**, *123*, 126204. [[CrossRef](#)]
51. Sun, L.; Wen, J.; Wang, J.; Zhao, Y.; Zhang, B.; Wu, J.; Xu, Y. Two-view attention-guided convolutional neural network for mammographic image classification. *CAAI Trans. Intell. Technol.* **2023**, *8*, 453–467. [[CrossRef](#)]
52. Tselka, I.; Detsikas, S.E.; Petropoulos, G.P.; Demertzi, I.I. Google Earth Engine and machine learning classifiers for obtaining burnt area cartography: A case study from a Mediterranean setting. In *Geoinformatics for Geosciences*; Elsevier: Amsterdam, The Netherlands, 2023; pp. 131–148.
53. Roy, P.K.; Saumya, S.; Singh, J.P.; Banerjee, S.; Gutub, A. Analysis of community question-answering issues via machine learning and deep learning: State-of-the-art review. *CAAI Trans. Intell. Technol.* **2023**, *8*, 95–117. [[CrossRef](#)]
54. Shamshiri, R.; Eide, E.; Høyland, K.V. Spatio-temporal distribution of sea-ice thickness using a machine learning approach with Google Earth Engine and Sentinel-1 GRD data. *Remote Sens. Environ.* **2022**, *270*, 112851. [[CrossRef](#)]
55. Wang, X.; Wang, S.; Chen, P.Y.; Lin, X.; Chin, P. Block switching: A stochastic approach for deep learning security. *arXiv* **2020**, arXiv:2002.07920. [[CrossRef](#)]
56. Stumpf, A.; Kerle, N. Object-oriented mapping of landslides using Random Forests. *Remote Sens. Environ.* **2011**, *115*, 2564–2577. [[CrossRef](#)]
57. Zhao, F.; Feng, S.; Xie, F.; Zhu, S.; Zhang, S. Extraction of long time series wetland information based on Google Earth Engine and random forest algorithm for a plateau lake basin—A case study of Dianchi Lake, Yunnan Province, China. *Ecol. Indic.* **2023**, *146*, 109813. [[CrossRef](#)]
58. Suryono, H.; Kuswanto, H.; Iriawan, N. Rice phenology classification based on random forest algorithm for data imbalance using Google Earth engine. *Procedia Comput. Sci.* **2022**, *197*, 668–676. [[CrossRef](#)]
59. Shakeel, N.; Shakeel, S. Context-Free Word Importance Scores for Attacking Neural Networks. *J. Comput. Cogn. Eng.* **2022**, *1*, 187–192. [[CrossRef](#)]
60. Choudhuri, S.; Venkateswara, H.; Sen, A. Coupling Adversarial Learning with Selective Voting Strategy for Distribution Alignment in Partial Domain Adaptation. *arXiv* **2022**, arXiv:2207.08145. [[CrossRef](#)]
61. Aji, M.A.P.; Kamal, M.; Farda, N.M. Mangrove species mapping through phenological analysis using random forest algorithm on Google Earth Engine. *Remote Sens. Appl. Soc. Environ.* **2023**, *30*, 100978. [[CrossRef](#)]

62. Bittencourt, H.R.; Clarke, R.T. Use of classification and regression trees (CART) to classify remotely-sensed digital images. In Proceedings of the 2003 IEEE International Geoscience and Remote Sensing Symposium, Toulouse, France, 21–25 July 2003; IEEE: Piscataway, NJ, USA, 2003; Volume 6, pp. 3751–3753.
63. Ghosh, S.; Kumar, D.; Kumari, R. Google earth engine based computational system for the earth and environment monitoring applications during the COVID-19 pandemic using thresholding technique on SAR datasets. *Phys. Chem. Earth Parts A/B/C* **2022**, *127*, 103163. [[CrossRef](#)]
64. Jia, Z.; Wang, W.; Zhang, J.; Li, H. Contact High-Temperature Strain Automatic Calibration and Precision Compensation Research. *J. Artif. Intell. Technol.* **2022**, *2*, 69–76.
65. Hu, X.; Kuang, Q.; Cai, Q.; Xue, Y.; Zhou, W.; Li, Y. A Coherent Pattern Mining Algorithm Based on All Contiguous Column Biclust. *J. Artif. Intell. Technol.* **2022**, *2*, 80–92. [[CrossRef](#)]
66. Li, J.; Li, L.; Song, Y.; Chen, J.; Wang, Z.; Bao, Y.; Zhang, W.; Meng, L. A robust large-scale surface water mapping framework with high spatiotemporal resolution based on the fusion of multi-source remote sensing data. *Int. J. Appl. Earth Obs. Geoinf.* **2023**, *118*, 103288. [[CrossRef](#)]
67. Bai, S.B.; Wang, J.; Lu, G.N.; Kanevski, M.; Pozdnoukhov, A. GIS-based landslide susceptibility mapping with comparisons of results from machine learning methods process versus logistic regression in Bailongjiang river basin, China. In *Geophysical Research Abstracts*; EGU General Assembly: Vienna, Austria, 2008; Volume 10, pp. 1–2.
68. Arabameri, A.; Roy, J.; Saha, S.; Blaschke, T.; Ghorbanzadeh, O.; Tien Bui, D. Application of probabilistic and machine learning models for groundwater potentiality mapping in Damghan sedimentary plain, Iran. *Remote Sens.* **2019**, *11*, 3015. [[CrossRef](#)]
69. Meng, J.; Li, Y.; Liang, H.; Ma, Y. Single-image dehazing based on two-stream convolutional neural network. *J. Artif. Intell. Technol.* **2022**, *2*, 100–110. [[CrossRef](#)]
70. Calasan, M.; Aleem, S.H.A.; Zobia, A.F. On the root mean square error (RMSE) calculation for parameter estimation of photovoltaic models: A novel exact analytical solution based on Lambert W function. *Energy Convers. Manag.* **2020**, *210*, 112716. [[CrossRef](#)]
71. Hamzhepour, N.; Bogaert, P. Improved spatiotemporal monitoring of soil salinity using filtered kriging with measurement errors: An application to the West Urmia Lake, Iran. *Geoderma* **2017**, *295*, 22–33. [[CrossRef](#)]
72. Peng, J.; Biswas, A.; Jiang, Q.; Zhao, R.; Hu, J.; Hu, B.; Shi, Z. Estimating soil salinity from remote sensing and terrain data in southern Xinjiang Province, China. *Geoderma* **2019**, *337*, 1309–1319. [[CrossRef](#)]

**Disclaimer/Publisher’s Note:** The statements, opinions and data contained in all publications are solely those of the individual author(s) and contributor(s) and not of MDPI and/or the editor(s). MDPI and/or the editor(s) disclaim responsibility for any injury to people or property resulting from any ideas, methods, instructions or products referred to in the content.